Aeolian Research 54 (2022) 100766

Contents lists available at ScienceDirect

Aeolian Research

journal homepage: www.elsevier.com/locate/aeolia

A North American dust emission climatology (2001–2020) calibrated to dust point sources from satellite observations

Mark Hennen [a,*], Adrian Chappell [a], Brandon L. Edwards [b], Akasha M. Faist [c], Tarek Kandakji [e], Matthew C. Baddock [d], Brandi Wheeler [b], Gayle Tyree [b], Ronald Treminio [b], Nicholas P. Webb [b]

[a] School of Earth and Environmental Sciences, Cardiff University, Cardiff CF10 3XQ, UK
[b] USDA-ARS Jornada Experimental Range, Las Cruces, NM, 88003, USA
[c] Department of Animal and Range Sciences, New Mexico State University, Las Cruces, NM, USA
[d] Geography and Environment, Loughborough University of Technology, Loughborough, UK
[e] Yale School of the Environment Yale University, New Haven, CT 06520, USA

ARTICLE INFO

Keywords:
Dust emission
Remote sensing
MODIS
Albedo
Land cover type
Ecoregions

ABSTRACT

Measurements of atmospheric dust have long influenced our understanding of dust sources and dust model calibration. However, assessing dust emission magnitude and frequency may reveal different dust source dynamics and is critical for informing land management. Here we use MODIS (500 m) albedo-based daily wind friction estimates to produce a new dust emission climatology of North America (2001–2020), calibrated by the novel use of dust point sources from optical satellite observations (rather than being tuned to dust in the atmosphere). Calibrated dust emission occurred predominantly in the biomes of the Great Plains (GP) and North American Deserts (NAD), in broad agreement with maps of aerosol optical depth and dust deposition but with considerably smaller frequency and magnitude. Combined, these biomes produced 7.2 Tg y^{-1} with contributions split between biomes (59.8% NAD, 40.2% GP) due to the contrasting conditions. Dust emission is dependent on different wind friction conditions on either side of the Rocky Mountains. In general, across the deserts, aerodynamic roughness was persistently small and dust sources were activated in areas prone to large wind speeds; desert dust emissions were wind speed limited. Across the Great Plains, large winds persist, and dust emission occurred when vegetation cover was reduced; vegetated dust emissions were roughness limited. We found comparable aerodynamic roughness exists across biomes/vegetation classes demonstrating that dust emission areas are not restricted to a single biome, instead they are spread across an 'envelope' of conducive wind friction conditions. Wind friction dynamics, describing the interplay between changing vegetation roughness (e.g., due to climate and land management) and changing winds (stilling and its reversal), influence modelled dust emission magnitude and frequency and its current and future climatology. We confirm previous results that in the second half of the 21st century the southern Great Plains is the most vulnerable to increased dust emission and show for the first time that risk is due to increased wind friction (by decreased vegetation roughness and / or increased wind speed). Regardless of how well calibrated models are to atmospheric dust, assuming roughness is static in time and / or homogeneous over space, will not adequately represent current and future dust source dynamics.

Introduction

Across North America, land use practices, land cover change, and climate change are influencing wind erosion and dust emission, often with profound regional impacts (Ravi et al., 2010; Hand et al., 2016). Locally, wind erosion is leading to substantial removal of soil, carbon, and other nutrients from vulnerable landscapes, negatively affecting cropland productivity (Zobeck et al., 2013) ecosystem function (Breshears et al., 2009; Field et al., 2010) and the provision of ecosystem services from managed lands (Okin et al., 2011; Webb et al., 2020). Increasing concentrations of aerosol dust are negatively impacting human health and livelihoods (Li et al., 2018), regional water supplies (Painter et al., 2018), and affecting the climate (Schepanski, 2018). Resolving the impacts of regional ecosystem and climate changes on aeolian processes is necessary to understand anthropogenic effects on landscapes and identify management options (Webb and Pierre, 2018).

* Corresponding author at: School of Earth and Environmental Sciences, Cardiff University, Room 1.37, Main Building, Park Place Cardiff CF10 3AT, UK.
E-mail address: hennenm@cardiff.ac.uk (M. Hennen).

https://doi.org/10.1016/j.aeolia.2021.100766
Received 2 July 2021; Received in revised form 10 November 2021; Accepted 11 November 2021
Available online 21 November 2021

Management options are now required to avoid further land degradation and desertification of ecosystems (Bestelmeyer et al., 2015), provide food security (Pimentel, 2000), reduce dust impacts on communities (UNEP UNCD, 2016,), and enable climate change adaptation and sustainable development of agroecosystems (Edwards et al., 2019; Webb et al., 2017a; Webb et al., 2017b). Identifying significant sources and spatio-temporal patterns of dust emission across North America is critical for understanding links between causal mechanisms and drivers of change across land use and cover types (Webb et al., 2017a; Webb et al., 2017b).

Our current understanding of the location and extent of regional North American dust sources was mainly established from satellite observations of aerosol optical depth (AOD) and ground-based aerosol monitoring networks. Prospero et al. (2002) and Ginoux et al. (2012) provided synoptic-scale analyses of persistent dust hotspots using Total Ozone Mapping Spectrometer (TOMS) and Moderate Resolution Imaging Spectroradiometer (MODIS) Deep Blue data, respectively. Those studies identified the North American deserts and Great Plains as the most likely dominant dust source areas. However, atmospheric dust concentrations are dependent on the varying magnitude and frequency of dust emission, dust transport and dust residence time, which combined, makes actual dust source contributions more complicated to identify. Finer-scale field monitoring and remote sensing analyses targeting dust point sources found similar regional patterns and revealed the spatio-temporal heterogeneity of dust source erodibility within the deserts and Great Plains (e.g., Lee et al., 2009; Baddock et al., 2011; Kandakji et al., 2020, b). Analyses of blowing dust observations (e.g., Orgill and Sehmel, 1976; Goudie, 1983; Goudie and Middleton, 1992), AOD (e.g., Eibedingil et al., 2021), and dust concentration data from ground-based monitoring networks (e.g., Hand et al., 2016) also show consistent regional patterns in the deserts and the Great Plains and have revealed trends in dustiness that suggest a substantial anthropogenic influence on dust emissions. Targeted field-based, remote sensing, and modelling studies support the case that ecosystem changes driven by land use and climate are changing the extent of North American dust sources and the magnitude of emissions (e.g. Li et al., 2013; Webb et al., 2014; Nauman et al., 2018).

To address the need for understanding dust source activity by land use and land cover types, we develop a climatology of dust emission across North America during the period January 2001 to December 2020, inclusive. We simulate at-source dust emission using a model that implements the MODIS albedo-based drag partition scheme developed by Chappell and Webb (2016; hereafter CW16) to resolve effects of heterogeneous and dynamic surface roughness on wind friction velocities. However, models continue to over-estimate dust emission with crude assumptions about threshold and the infinite supply of dry, loose erodible material. To overcome these long-standing assumptions and better constrain the modelling, we implement a novel calibration of the dust emission model using published dust point source observations from satellite observations. We then identify spatial and temporal patterns of dust emission among different north American ecoregions and elaborate where and when modelled dust emissions are responding to changes in aerodynamic roughness and wind speed (wind friction). Our analysis provides the first comprehensive assessment of the location and intensity of North American dust emission sources and change (not to be confused with dust in the atmosphere).

Data and methods

CW16 dust emission model

We calculated daily dust emission F (kg m^{-2} y^{-1}) and made annual average estimates using the albedo-based approach developed by Chappell and Webb (2016). Dust emission models rely on estimates of saltation flux Q (g m^{-1} s^{-1}) to predict F. The Q for a given particle diameter (d), soil moisture (w), wind speed (U_h), and albedo (ω) were calculated as

$$Q(d,w,\omega,U_h) = c\frac{\rho_a}{g}u_{s*}^3(\omega,U_h)\left(1+\frac{u_{*ts}(d)H(w)}{u_{s*}(\omega,U_h)}\right)\left(1-\left(\frac{u_{*ts}(d)H(w)}{u_{s*}(\omega,U_h)}\right)^2\right) \quad (1)$$

where ρ_a is air density (1.23 kg m^{-3}), g is gravitational acceleration (9.81 m s^{-2}), c is a dimensionless fitting parameter (set to 1), $u_{*ts}(d)$ is threshold wind friction velocity (m s^{-1}). Soil surface wind friction velocity (hereafter wind friction) u_{s*} describes wind shear stress acting on the soil following attenuation of momentum by roughness elements at all scales (topography, vegetation, soil). The $H(w)$ is a correction for soil moisture following Fécan et al. (1999). The definition of u_{*ts} follows (Marticorena and Bergametti, 1995) as described in the workflow of Darmenova et al. (2009). The above equation (Eq. (1)) describes how the magnitude of sediment transport is calculated and adjusted by the frequency of occurrence (0 or 1) i.e., $u_{s*} > u_{*ts}$, and if transport occurs then the magnitude is attenuated by $H(w)$ and u_{s*} available at the soil surface.

Calculation of u_{s*} from wind speed U (m s^{-1}) at a single height h (m) requires a description of the aerodynamic roughness of the surface. CW16 uses daily black sky albedo (ω) measurements from Moderate-resolution Imaging Spectroradiometer (MODIS) (MCD43A3 v6) data (500 m resolution) to represent aerodynamic roughness as the proportion of shelter approximated using shadow (1-ω) (Chappell and Webb, 2016). Following CW16, the u_{s*} per pixel per day is calculated by:

$$\frac{u_{s*}}{U_h} = 0.0311\left(exp\frac{-\omega_{ns}{}^{1.131}}{0.016}\right)+0.007 \quad (2)$$

where u_{s*}/U_h from Marshall (1971) reconstructed from wind tunnel experiments is related empirically to shadow (reciprocal of black-sky albedo; ω), spectrally normalized (ω_n) using the MODIS isotropic parameter f_{iso} , to remove the spectral influence of the observed surface (e.g., colour, material, moisture content) and then rescaled (ω_{ns}) from a MODIS range ($\omega_{nmin} = 0$, $\omega_{nmax} = 35$) for a given illumination zenith angle ($\theta = 0^{\circ}$). To describe conditions of U_h during sediment transport, the daily maximum wind speed at $h = 10$ m above the soil surface was obtained from ECMWF Climate Reanalysis, ERA5-Land hourly wind field data at 11 km spatial resolution (Muñoz Sabater, 2019). The ratio between u_{s*} and U_h describes relative aerodynamic roughness (u_{s*}/U_h) independent of wind speed (Fig. 1).

Dust emission F (kg m^{-2} s^{-1}) is calculated as:

$$F(d) = A_f A_s M Q(d) 10^{(13.4\%_{clay}-6.0)} \quad (3)$$

We allowed $\%_{clay}$ to realistically vary spatially but with the restriction $\max(\%_{clay}) = 20$. We recognise that restricting $\%_{clay}$ to a maximum value of 20% has produced reasonable results when applied in regional models. The proportion of emitted dust in the atmosphere M for a given size fraction (d). We calculated the relative surface area (M). In each pixel, the coverage of snow (A_s) and whether the soil surface is frozen (A_f) is used to reduce dust emission and is obtained from daily ERA5-Land data. Unlike existing dust models, the use of ω_{ns} to dynamically estimate u_{s*} removes the need for vegetation indices and fixed vegetation coefficients to determine effective aerodynamic roughness. Furthermore, because u_{s*} is spatially explicit, it is not necessary to apply preferential dust source masks to pre-condition F (i.e., increasing F in areas perceived to have greater erodibility).

Dust emission model calibration

Typically, dust model calibration relies on either ground-station data that are often not collected at dust sources (e.g., Dubovik et al., 2000) or satellite observations of aerosol optical depth (AOD) (e.g., Eck et al., 1999; Carboni et al., 2012). Each of these data have inherent limitations, linked to the lack of spatial resolution or frequency of observation. Importantly, neither dust concentrations nor AOD pertain exclusively to

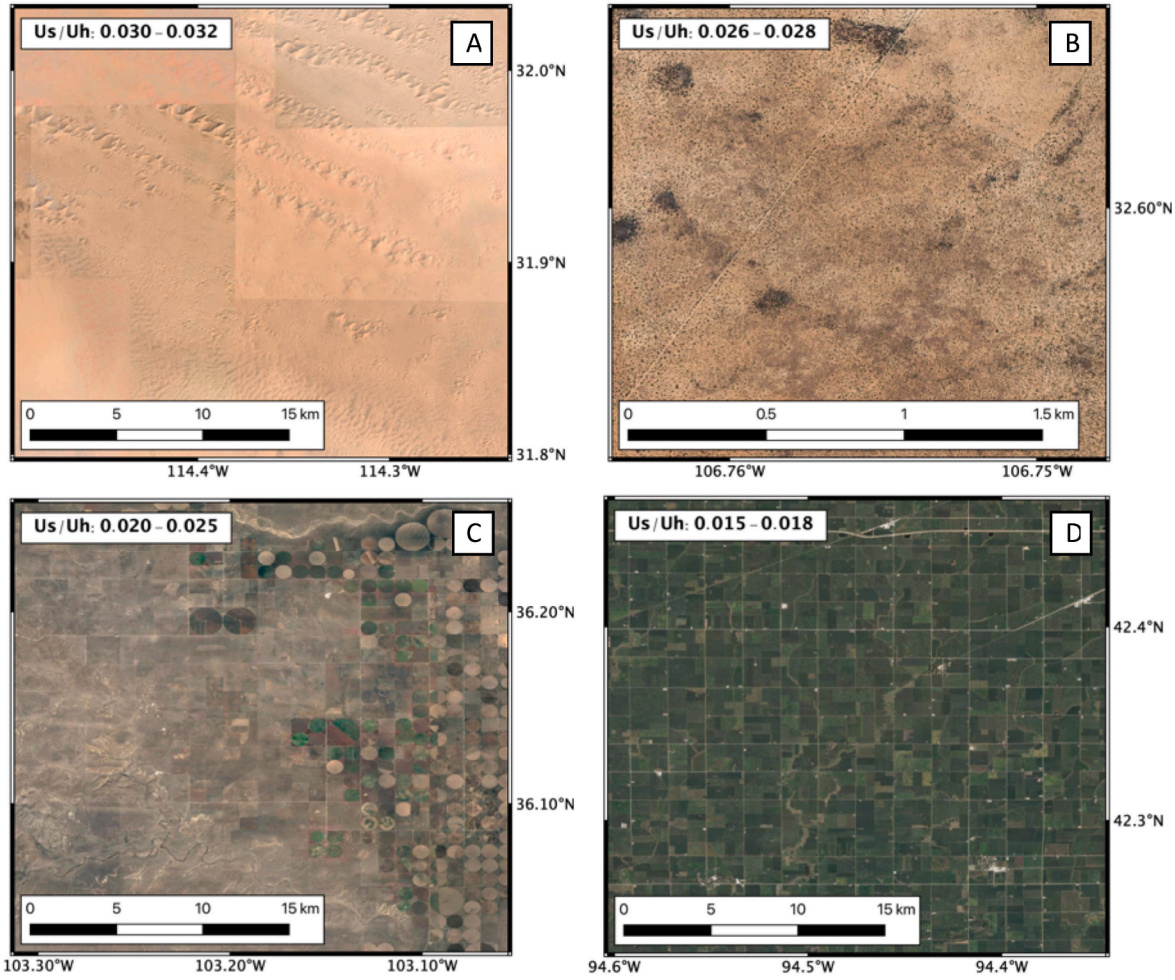

Fig. 1. Surface conditions in areas of different aerodynamic roughness ($\frac{u_{s^*}}{U_h}$) located in Fig. 2. Areas A-D show vegetation cover in areas with specified roughness measurements.

observations of emission, with both capturing advected dust that has been transported some distance from source and resides in the atmosphere for some time. Thus, dust emission model calibration using AOD, or dust concentrations will ensure dust loads are calibrated, but given the range of factors influencing dust loads, the location of source areas and magnitude of emissions from various sources may be incorrect and / or biased to those dust sources which have long atmospheric residence times (Huneeus et al., 2011).

Here we tackle this long-standing discrepancy in dust emission model calibration. We use satellite observed dust emission point source (DPS) observations of dust emission frequency, identified through visual inspection of satellite data by Baddock et al. (2011), Lee et al., 2009, and Kandakji *et al.* (2020a) to calibrate CW16. Human interpretation of satellite data provides many advantages compared to automated approaches (Schepanski et al., 2012). Through pattern recognition, the human eye is adept at delineating the point at the head of a dust plume, especially where the dust plume is spectrally like bare ground (Hennen et al., 2019). Disadvantages related to image sampling frequency and occasional opaque atmosphere due to clouds or atmospheric dust are unavoidable. However, in the absence of extensive networks providing dust emission measurements, DPS data provide the best available and most proximal data for calibrating the location and timing of dust emission. Accordingly, we calibrate F estimates by comparing published dust source observations to modelled F. First, we calculated the DPS probability of occurrence P(DPS > 0), a first order approximation of the probability of sediment transport P($Q > 0$), which is directly proportional to dust (F) emission P($F > 0$) at those locations. Next, we equated this to study durations equal to the frequency u_{s^*} exceeds u_{*ts} adjusted by $H(w)$

$$P(DPS > 0) \approx P(Q > 0) \propto P(F > 0) = u_{s^*} > u_{*ts} H(w) \begin{cases} 1 \\ 0 \end{cases} \quad (4)$$

Accurate estimates of the magnitude and frequency of F depend on correctly predicting P($F > 0$), which itself depends on $u_{*ts}H(w)$. However, the dust emission scheme (specifically u_{*ts}) assumes that the soil surface is uniform and covered with an infinite supply of loose erodible material, which when mobilised by sufficient wind friction (at the surface u_{s^*}) causes dust emission. This (energy limited) assumption is rarely justified in dust source regions where the soil surface is rough due to soil aggregates, rocks, or gravel, sealed with biological or physicals crusts, or loose sediment is simply unavailable. We address this weak assumption using the observed dust emission frequencies at DPS data locations. Furthermore, we reduced the reported uncertainty associated with the precise location of the dust emission point sources by aggregating over 1° grid boxes. We calculated daily (mean kg m^{-2} y^{-1}) dust emission values (Eqs. (1) & (3)) for locations, when and where DPS observations identified dust (sediment transport occurred).

$$Q = C \frac{\rho_a}{g} u_{s^*}^3 P(DPS > 0) \quad (5)$$

We compare those estimates with dust emission determined by CW16. Both observed and modelled DPS emission values and

frequencies are aggregated within a 1°x1° grid cell, where a mean value is calculated from all DPS locations that intersect that grid cell. The mean difference between the pairs of data (i) is described by the root-mean-square-difference (RMSE),

$$RMSE = \sqrt{\frac{\sum_{i=0}^{n}(S_i - O_i)^2}{n - df}} \quad (6)$$

where n is the number of grid boxes, S is modelled, and O observed values for each grid box, and degrees of freedom (df) describe the number of independent variables in the calculation of F (here $df = 9$; Eq. (1) and Eq. (3)). We use only half of the available grid box data to fit the functions. We sampled half of the available data by systematically stratifying across the log-scale, with random selection within each stratum. We reserved the unused half of these data to validate the calibration of CW16. The quality of the validation demonstrates the ability of the calibration for only a small portion of North America to be predicted elsewhere. This novel approach enables routine adjustment of dust emission model predictions by DPS observed frequency of occurrence whilst u_{*ts} remains poorly constrained in dust emission modelling.

North American dust emission climatology (2001–2020)

We used the Google Earth Engine parallel computing to run the CW16 model utilising the catalogue of MODIS and ERA5-Land data. We produced daily estimates of dust emission at 500 m spatial resolution (visualised in maps at 5 km pixels) for North America during the period January 2001 to December 2020, inclusive. Model estimates were spatially classified by ecological units (Fig. 2) to characterise geographic and vegetation dependencies in patterns of dust emission, wind, and aerodynamic roughness. The Environmental Protection Agency (EPA) level II ecological classification scheme divides the region into 22 ecoregions, which are grouped into four vegetation-type biomes (shown previously in Fig. 1 including desert (barren), shrubland, short grass prairie and tall grass prairie; Omernik, 1987). Ecoregions were used to identify distinct areas of large dust emission potential and explain between- and within-group variance in dust emission, surface aerodynamic roughness, and wind speed.

Results

Model calibration

The satellite observed dust emission point sources (DPS) from three published datasets describe the dust emission frequency across the Southern High Plains and northern Chihuahuan Desert in southwest North America (Fig. 3b & 3d). The DPS observations and modelled outputs were aggregated into 1° grid boxes (Fig. 3b & 3d), preventing any inconsistency due to subjective dust source identification affecting the comparison. Sample locations within each dataset were stratified across all probability and dust emission values (Fig. 3b & 3d) to maintain consistency in the correlation across all ranges of dustiness. We reserved the other half of the data to validate the model. Observed DPS frequency and modelled dust emission ($F > 0$) frequency are presented in Fig. 3a, where modelled frequency (mean 12.3 days/y) exceeds observed frequency (mean 0.02 days/y) by two orders of magnitude ($R^2 = 0.85$). Mean modelled dust emission (F; kg m^{-2} y^{-1}) on observed DPS days only, were compared with modelled F on all days (Fig. 3c). Modelled estimates exceeded observations, with an RMSE modelled F = 140.8 kg m^{-2} y^{-1} (with an $R^2 = 0.74$) greater than those from DPS days. Using the remaining 50% of grid boxes from each dataset, we calibrated the modelled frequency and dust emission on all days, to those on DPS days. We used linear regression of log data to calibrate modelled P($F >$ 0):

$$Log_{10}(P_{cal}) = 0.49 Log_{10}(P) - 2.17 \quad (7)$$

and modelled F:

$$Log_{10}(F_{cal}) = 0.88 Log_{10}(F) - 2.02 \quad (8)$$

where F_{cal} and P_{cal} are the adjustment of modelled values using these calibrations. Our approach provides for the first time a calibration of large area dust emission consistent with satellite observed dust emission. It assumes, like other large area estimates of dust emission, that the magnitude of dust emission does not need to be adjusted i.e., $C = 1$. With its use of DPS, this approach overcomes the currently poor model constraint of the sediment transport threshold u_{*ts} . It should be noted that DPS data is very likely biased away from the smallest dust sources which may not appear or are difficult for operators to detect using

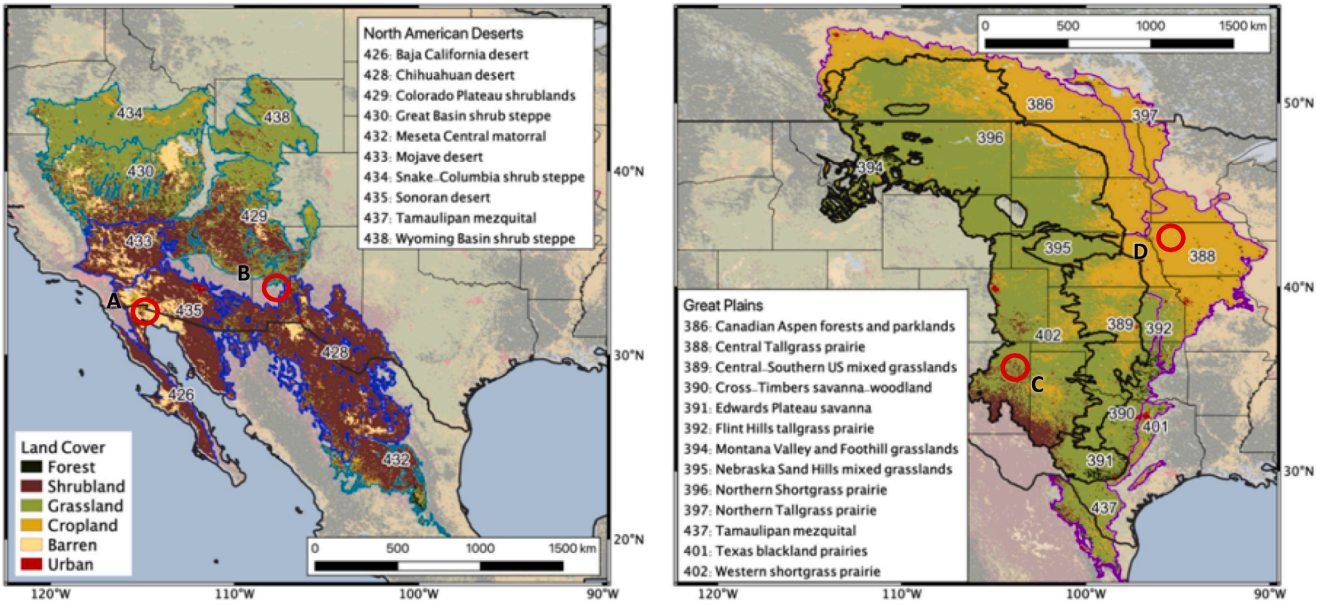

Fig. 2. Ecological regions of the Great Plains and North American Deserts. Red circles identify the location of the images showing land surface roughness (Fig. 1). Source: RESOLVE (Dinerstein et al., 2017**).** (For interpretation of the references to colour in this figure legend, the reader is referred to the web version of this article.)

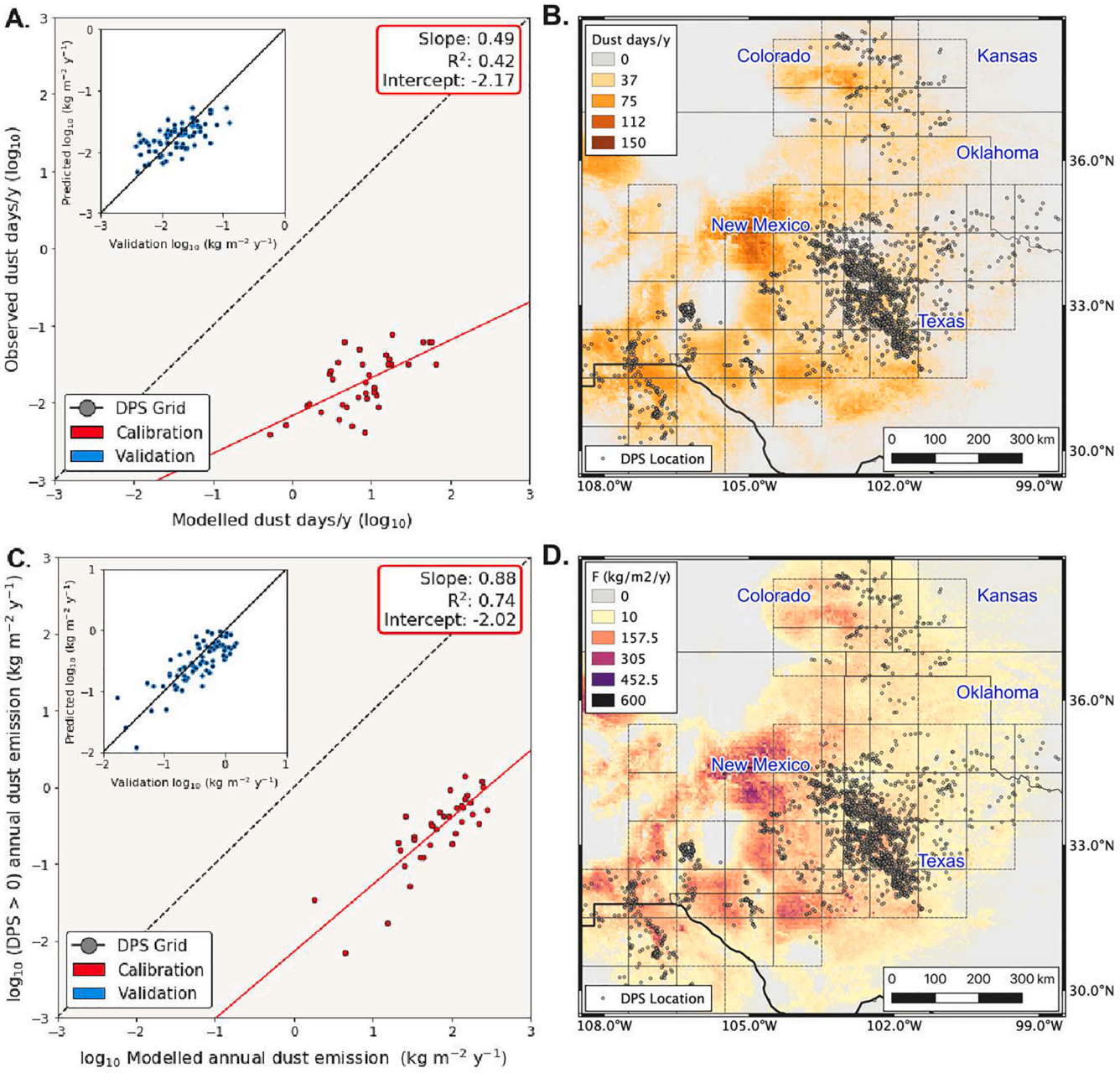

Fig. 3. Comparison of observed and modelled dust emission frequency ($F > 0$) and magnitude (F). The albedo-based annual (2001–2020) average dust emission frequency (A) and magnitude (C) at dust point source (DPS) locations (i.e., panel B and D) on observed DPS days (y-axis) and all days during observation period (x-axis). The dashed line is the 1:1 line. The inset plot shows the validation of the calibration function fitted to albedo-based dust emission values. Uncalibrated modelled average annual dust emission frequency (B) and magnitude (D) in the region of the DPS locations. DPS locations include results from Lee et al. (2012); Baddock et al. (2011); Kandakji et al. (2020).

optical reflectance (Urban *et al.*, 2018). Under these assumptions, the calibrated model (F_{cal}) provides precise and accurate maps of seasonal dust emission, temporal dynamics and mean regional dust emission without tuning to atmospheric optical measurements.

Spatial and seasonal patterns of North American dust emission 2001–2020

Fig. 4 presents the mean annual dust emission and frequency of days per year where F_{cal} >0 kg m^{-2} y^{-1} across North America during the period 2001 to 2020. We found F_{cal} was almost entirely (98% of all dust emission) produced from two biomes: the North American Deserts (NAD) and Great Plains (GP) regions. Combined, the regions generated on average 7.2 Tg y^{-1} (59.8% NAD, 40.2% GP), with a mean dust emission per unit area of 0.08 kg m^{-2} y^{-1} (0.12 and 0.06 kg m^{-2} y^{-1} for NAD and GP respectively). The F_{cal} had large spatial variability within each region, with the largest concentration of dust source areas occurring in a central corridor surrounding the Central Rocky Mountains (Fig. 4). Dust emission occurred most frequently across the Southern High Plains (southwest GP), northern Chihuahuan Desert, and southwest Colorado Plateau and the Great Divide Basin within the Wyoming Basin. Short grass prairies contributed the most dust by biome (2.86 Tg y^{-1}), followed by shrublands (2.4 Tg y^{-1}), deserts (1.89 Tg y^{-1}), and tall grass prairies (0.02 Tg y^{-1}) (Table 1). Deserts produced the highest mean dust frequency (10 dust days per year / 1° grid box), followed by shrublands (7.5), short grass prairies (7.4) and tall grass prairies (1.9).

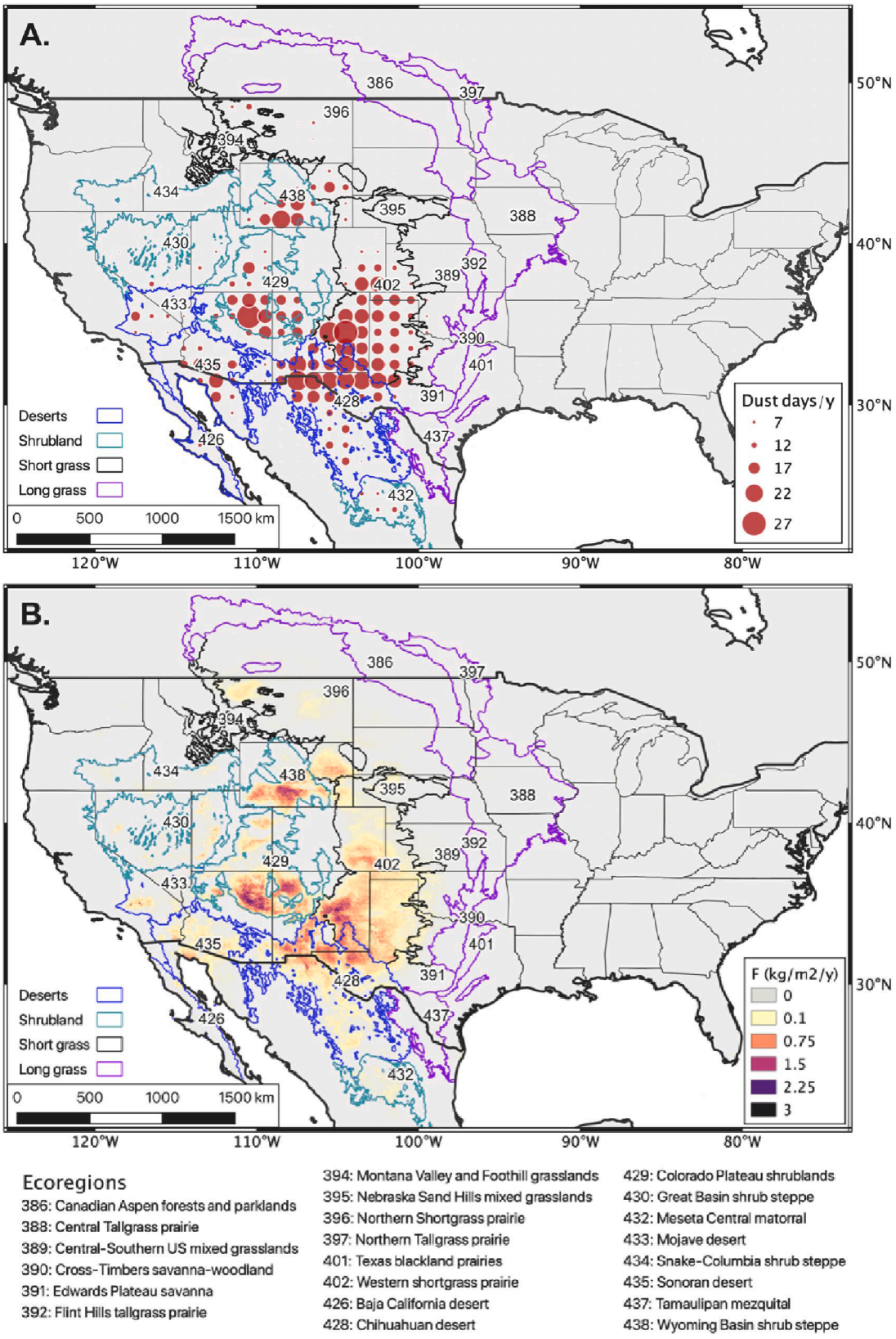

Fig. 4. Calibrated dust emission (F_{cal}) frequency (a - Eq.7) and dust emission magnitude (b - Eq.8) across North America during the period 2001 – 2020 as estimated from the albedo-based dust emission model. MODIS pixel (500 m^2) dust days per year are calibrated using Eq.7 and aggregated by 1° grid.

Table 1
Descriptive statisitics of calibrated dust emission (F_{cal}) magnitude, frequency, and wind speed (U_h) of North American biomes for the period 2001–2021. Source of U_h = ECMWF (ERA5-Land).

Biome	Total F_{cal} (Tg y^{-1})	Mean F_{cal} (kg m^{-2} y^{-1})	Stdev F_{cal} (kg m^{-2} y^{-1})	Mean Freq. (dust days/y)	Stdev Freq. (dust days/y)	Mean U_h (ms^{-1})	Stdev U_h (ms^{-1})
Desert	1.89	0.118	0.195	10.0	6.2	4.0	1.0
Shrubland	2.41	0.122	0.268	7.5	5.7	4.0	1.1
Short Grass	2.87	0.080	0.161	7.4	5.2	5.2	0.9
Tall Grass	0.03	0.004	0.006	1.9	1.4	4.5	0.6

Shrublands produced the most dust by area (0.12 kg m^{-2} y^{-1}) with the largest spatial variability or standard deviation of F (0.26 kg m^{-2} y^{-1}), followed by deserts (0.12 kg m^{-2} y^{-1}), short grass prairies (0.08 kg m^{-2} y^{-1}), and tall grass prairies (0.004 kg m^{-2} y^{-1}) where spatial variability was smaller (0.19, 0.16 and 0.006 kg m^{-2} y^{-1}, respectively). Spatial variability by ecoregion showed the Western shortgrass prairie ecoregion produced the largest total dust emission (2.22 Tg y^{-1}), followed by the Chihuahuan Desert (1.5 Tg y^{-1}) and Colorado Plateau (1.45 Tg y^{-1}) (Table 2). Of the 22 ecoregions, 15 produced total dust emission<0.1 Tg y^{-1}, including the Mojave and Baja California Deserts, Great Basin, Mesata Central Matorral and Snake Columbia shrublands, and all tall and short grass prairies except Western and Northern shortgrass prairie ecoregions. Nine ecoregions produced a mean dust emission frequency<4 (dust day per year for a MODIS pixel), including all tall grass prairie ecoregions, Montana Valley and Foothill grasslands and Snake-Columbia shrub steppe. The shrublands of the Colorado Plateau and Wyoming Basin produced the largest dust emission per unit area (0.262 and 0.255 kg m^{-2} y^{-1}, respectively), each with large spatial variability (standard deviation = 0.38 and 0.34 kg m^{-2} y^{-1}, respectively). Patterns of mean dust activation frequency followed those of dust emission magnitude, with the Western shortgrass prairie (13.4 dust days per year/1° grid), followed by the Chihuahuan Desert highest (12.2), Colorado Plateau (11.8), and Wyoming Basin (11.1).

Spatial variability in mean u_{s*}/U_h and U_h are shown in Fig. 5. As the biomes very well describe vegetation patterns, within-biome variability of u_{s*}/U_h was visually small in all biomes (<0.2 10^{-4}), while variability between biomes was visually distinct (Fig. 5b). Barren environments within deserts (e.g., Fig. 1a) had the largest mean u_{s*}/U_h (0.025), representing the lowest attenuation of U_h due to vegetation. The u_{s*}/U_h decreased in other biomes, as u_{s*} was increasingly reduced (relative to U_h) in response to vegetation cover increasing (shrub and grasslands), and / or vegetation structure becoming increasingly taller (tall grass and trees) (Fig. 1b-d). Accordingly, deserts had the largest mean u_{s*}/U_h compared with shrublands (0.023), short grass (0.02), and tall grass (0.016) prairies. The two grassland biomes of the Great Plains were distinguished by increasing roughness towards the east, as arid shrub, and patchy grassland transition over space into more continuous grassland and arable lands.

Spatial variability in mean U_h varied between the GP and NAD regions (Fig. 5a), as both short and long grass prairies observed higher mean wind speeds (5.2 and 4.5 m s^{-1}, respectively) than deserts and shrublands (both 4.0 m s^{-1}). Both GP and NAD produced discreet peaks in U_h of 8.3 m s^{-1} on the Southern High Plains (GP) and Wyoming Basin (NAD) respectively (Fig. 5a).

Seasonal patterns of F, u_{s*}/U_h, and U_h in each of the 22 ecoregions are shown in Fig. 6, these were shown as monthly anomalies against the annual mean (Table 1), normalising the varying magnitude between each ecoregion. Comparisons between mean monthly F showed variation between biomes, with most seasonal variability (+/- 0.2 kg m^{-2} y^{-1}) in the shrublands of the Wyoming Basin and Colorado Plateau, and the least seasonal variability in the desert ecoregions. In the Chihuahuan Deserts, Colorado Plateau and Western Shortgrass Prairie, F_{cal} peaked during March-May (MAM), while in most other ecoregions F_{cal} reached a maximum during December, January, and February (DJF). Minimum F_{cal} typically occurred during June-August (JJA), with small variability between ecoregions within the four biomes. The magnitude of u_{s*}/U_h variability was consistent within the biomes, with deserts and shrublands having a smaller range of roughness conditions than short and tall

Table 2
Calibrated dust emission magnitude (F_{cal}) and frequency ($F > 0$) for the 22 ecoregions of the Great Plains and North American Deserts.

Biome	Eco Region	Total F_{cal} (Tg y^{-1})	Mean F_{cal} (kg m^{-2} y^{-1})	Stdev F_{cal} (kg m^{-2} y^{-1})	Mean Freq. (dust days/y)	Stdev Freq. (dust days/y)
Deserts	*426: Baja California desert*	0.0095	0.016	0.032	5.2	3.0
	428: Chihuahuan desert	1.5012	0.169	0.238	12.2	6.6
	433: Mojave desert	0.0587	0.043	0.096	8.5	3.8
	435: Sonoran desert	0.2153	0.075	0.095	8.8	5.8
Shrublands	*429: Colorado Plateau shrublands*	1.4564	0.262	0.376	11.8	6.0
	430: Great Basin shrub steppe	0.0661	0.021	0.049	4.5	2.8
	432: Meseta Central matorral	0.0255	0.028	0.030	7.9	3.4
	434: Snake-Columbia shrub steppe	0.0192	0.012	0.019	3.6	1.7
	438: Wyoming Basin shrub steppe	0.6405	0.255	0.335	11.1	6.7
Short grass	*389: Central-Southern US mixed grasslands*	0.0703	0.022	0.031	5.5	2.5
	391: Edwards Plateau savanna	0.0216	0.035	0.060	4.3	4.1
	394: Montana Valley and Foothill grasslands	0.0027	0.008	0.012	1.6	1.7
	395: Nebraska Sand Hills mixed grasslands	0.0221	0.032	0.038	6.1	1.6
	396: Northern Shortgrass prairie	0.3480	0.029	0.061	5.3	2.7
	402: Western shortgrass prairie	2.2213	0.218	0.246	13.4	5.2
Tall grass	*386: Canadian Aspen forests and parklands*	0.0100	0.004	0.003	1.9	0.9
	388: Central Tallgrass prairie	0.0098	0.005	0.005	1.9	1.5
	390: Cross-Timbers savanna-woodland	0.0012	0.004	0.006	1.3	1.0
	392: Flint Hills tallgrass prairie	0.0003	0.002	0.002	3.5	0.4
	397: Northern Tallgrass prairie	0.0003	0.002	0.002	0.8	0.7
	401: Texas blackland prairies	0.0002	0.002	0.004	0.6	0.4
	437: Tamaulipan mezquital	0.0034	0.005	0.012	2.8	2.1

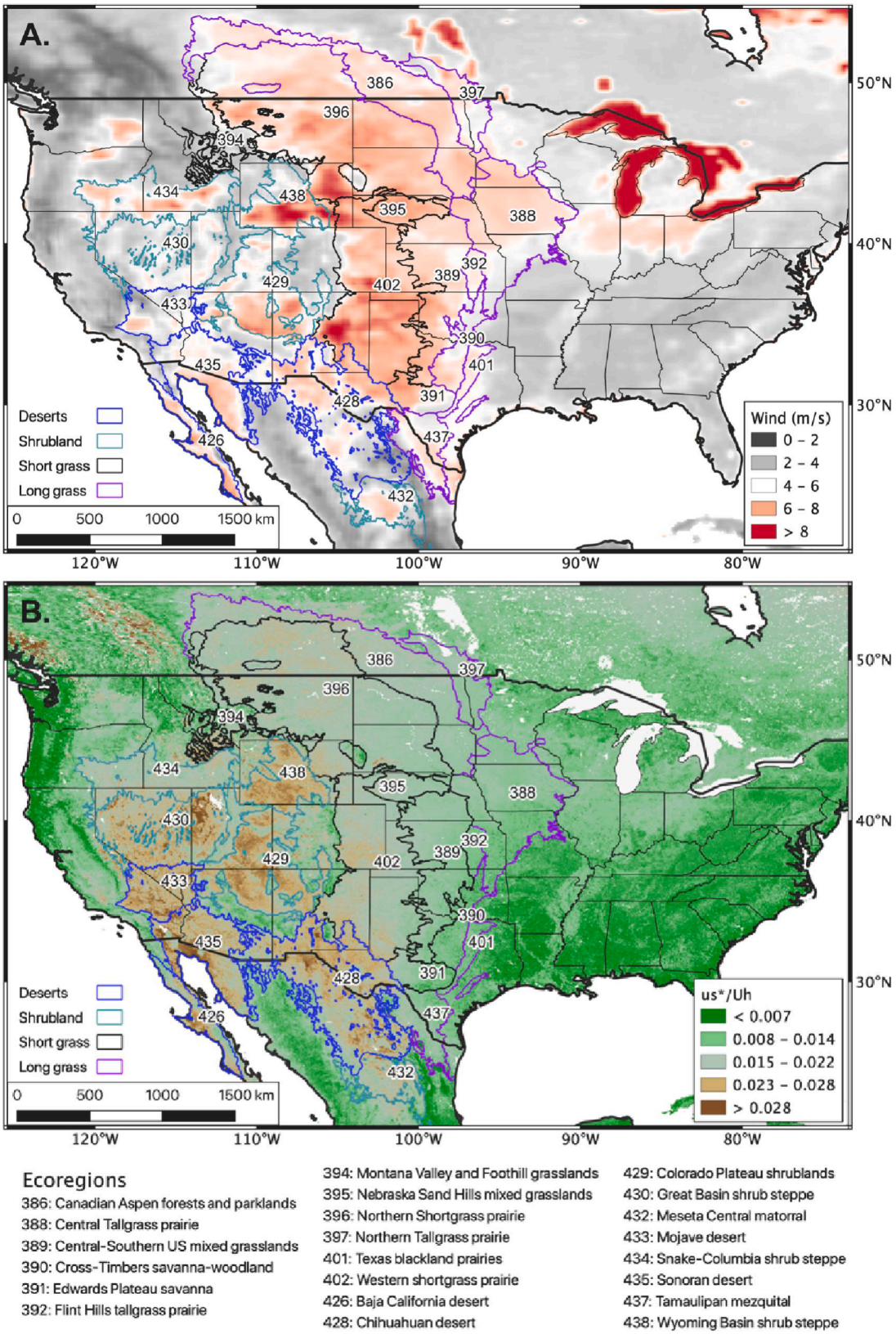

Fig. 5. Wind and roughness spatial variability across RESOLVE eco-regions of the Great Plains and North American Deserts.

grass prairies. Ecoregions in short and tall grass prairies had a maximum u_{s*}/U_h during December to February (DJF), with the ensuing decrease in u_{s*}/U_h (increasing roughness) during MAM or JJA, reflecting the deciduous pattern of vegetation in temperate climates. In all biomes, peak U_h tended to occur during MAM and decreased to a minimum in JJA, varying between 1 and 2 m s^{-1}.

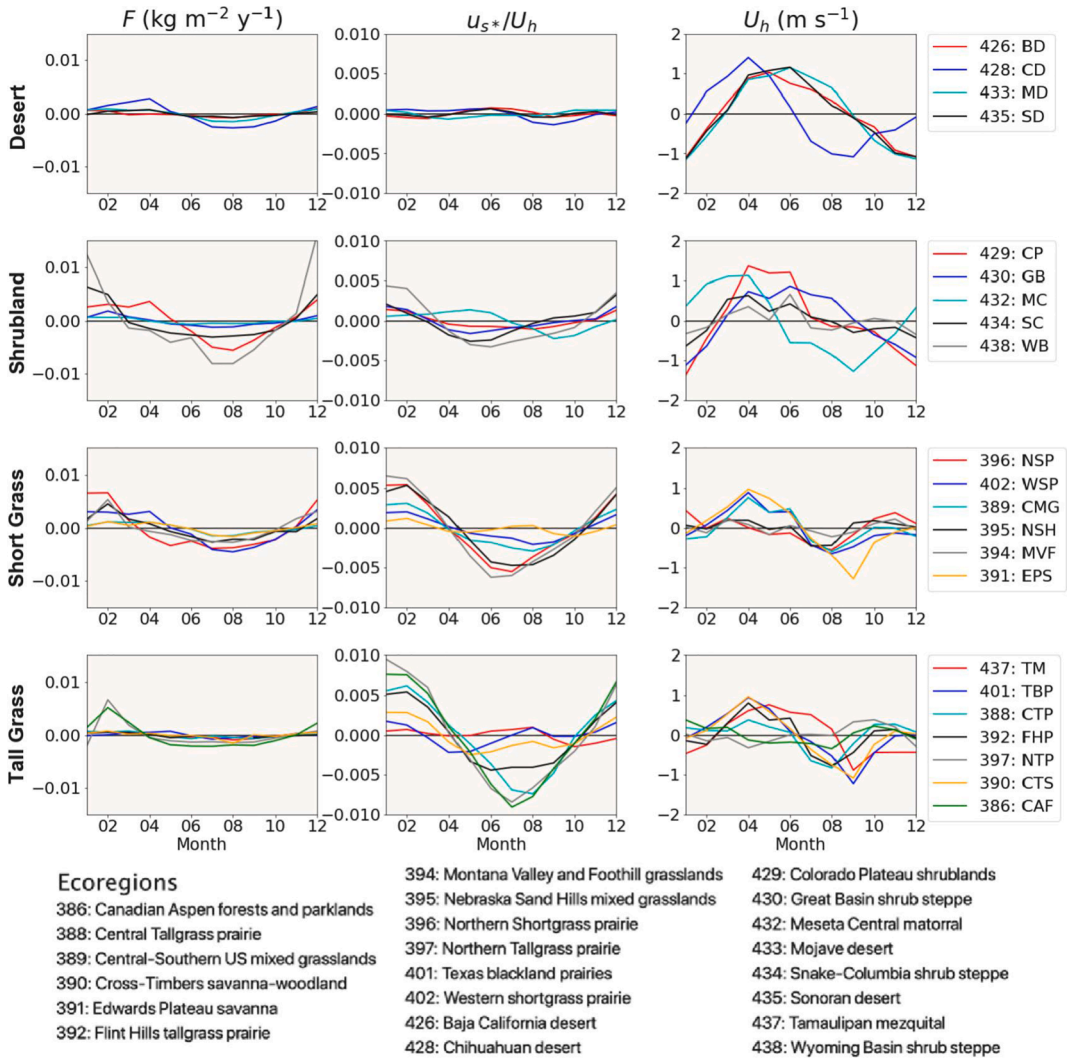

Fig. 6. Monthly anomalies of calibrated dust emission (F_{cal}), roughness (u_{s*}/U_h) and wind speed (U_h) for North America ecoregions (RESOLVE), grouped into biomes.

Discussion

Our results describe two distinct patterns of wind and surface roughness conditions, which coincide in different ways to generate changes in dust emission. Calibrated modelled dust emission in the Great Plains is limited by fluctuations in roughness, occurring only over areas of small vegetation roughness (Fig. 4) as winds were strong enough to produce dust emission most of the time (roughness limited) (Fig. 5). In contrast, dust emission over North American Deserts is wind speed limited, occurring only in exposed areas where wind speeds peak (Fig. 4) as surface roughness is small most of the time (wind limited) (Fig. 5). Despite these contrasting conditions, both biomes produced large volumes of dust (short grass prairie = 2.9 Tg y^{-1}, deserts and shrublands combined = 4.3 Tg y^{-1}). These modelled and calibrated dust emission values agree broadly with patterns described in previous literature, while explicitly describing only dust emission, not dust transport or deposition.

Previous studies identified an increase in daily frequencies of AOD (over a given threshold) over western areas of the GP, the Southern High Plains, Sonoran, and Mojave deserts (Pu and Ginoux, 2017; Ginoux et al., 2012). According to the CW16 model, the magnitude of F (Fig. 4b) varies spatially due to both the frequency of ($F_{cal} > 0$) and the associated mean wind speed attenuated by surface roughness (wind friction velocity (u_{s*}; m s^{-1}) – Eq. (2)). Here, our results correspond with fine-dust (FD) and course-mineral (CM) dust products, measured from the Interagency Monitoring of Protected Visual Environments (IMPROVE) ground station network (Hand et al., 2017). The CM peaks (15.1 mg m^{-3}) during MAM over the Southern High Plains in North Texas / New Mexico, contributing up to 72% of local PM_{10} mass. The FD concentrations peak (2.5 mg m^{-3}) during MAM over large areas of the Chihuahuan and Sonoran Deserts contributing up to 50% of $PM_{2.5}$ by mass (Hand et al., 2017).

North American Deserts: Interplay of vegetation structure and dynamic wind speeds

The EPA Desert (barren) biome incorporates four deserts of North America (Mojave, Chihuahuan, Sonoran and Baja). Described as arid or semi-arid landscapes, these ecoregions have limited precipitation, high temperatures and periodic droughts (Omernik, 1987). Their vegetation patterns remain consistent between seasons (Fig. 6) with desert scrub providing limited aerodynamic roughness (mean u_{s*}/U_h = 0.027 – 0.029) over much of the biome (Fig. 5). This is a testimony to the similarity between the ecoregion classification and the reduced complexity description of the aerodynamic roughness, indicating differences in the structural diversity of vegetation among the regions (LaRue et al., 2019). Despite these broad similarities, each ecoregion presented distinctly different dust emission. The Chihuahuan Desert ecoregion produced the greatest dust emission by magnitude (79% of biome total), and mean number of dust days (Table 2). Dust emission variability followed a

distinct north–south divide, where sediment transport was limited to areas in the north (eastern New Mexico / west Texas). This pattern followed synoptic patterns of U_h, which increased to a mean $U_h = 4.5 – 5.7$ m s^{-1} (Fig. 5a), as frequent cyclonic activity to the northeast (Albuquerque lows) creates large frontal systems with south-westerly winds (Rivera Rivera et al., 2009). Low-relief alluvial and playa surfaces, including Lake Palomas produce limited aerodynamic drag, generating the largest modelled dust emission (1.4 kg m^{-2} y^{-1} - Fig. 4 in agreement with previous dust emission observations studies (Fig. 2; Baddock et al., 2011; Lee et al., 2009). Areas to the south of the Chihuahuan Desert present broadly similar roughness conditions (mean $u_{s*}/U_h = 0.25–0.29$ – Fig. 5), yet the absence of frequent high U_h prevent frequent dust emission. These conditions are typical of desert ecoregions in North America.

The Mojave Desert was the most barren of the desert ecoregions (mean $u_{s*}/U_h = 0.027$), occupying a rain-shadow, shielded by the surrounding mountain ranges from advected humid air masses of the Pacific Ocean (Hereford et al., 2006). However, small mean U_h (3.5 m s^{-1}) limits modelled dust activity to several discrete locations, including numerous dry lakes, distal alluvial fans and ephemerally active washes surrounding the Rogers, Harper, and Coyote Lakes (117.2 – 116.8°W 35°N) within the Mojave National Preserve. These finding are consistent with previous observations in the literature (e.g., Frank et al., 2007; Sweeney et al., 2011). Here, mean U_h accelerates to ~ 5 m s^{-1} over barren surfaces ($u_{s*}/U_h > 0.3$), promoting frequent sediment transport (up to 17 dust days/y), equalling the peak frequency observed across North America (Fig. 4a). However, the small peak in mean wind speeds (Fig. 5b) limit dust emission to only small magnitudes (Fig. 4b).

Akin to deserts, modelled dust emission across shrubland ecoregions to the north tend to be wind speed limited. These diverse environments range from the arid and semi-arid deserts of the Colorado Plateau, and the Great Basin, to the grasslands and dense shrublands of the Snake-Columbia shrub steppe, and Wyoming Basin, with u_{s*}/U_h conditions ranging from 0.032 (barren) to 0.019 (grasslands) (Fig. 5). Wind speeds increase with passing cold fronts, driven by Pacific low-pressure systems traversing west to east bringing strong south-westerly winds (Jewell and Nicoll, 2011; Reynolds et al., 2016). Complex topography creates dynamic wind patterns, accelerating over exposed areas (ridges, valley floors), where average U_h exceeds 5 m s^{-1} (Fig. 5). Accordingly, modelled F increases across barren exposed areas, including Great Salt Lake Desert (116.8°W, 35.1°N) in eastern Great Basin, San Juan Basin (108.7°W, 36.5°N) and Hopi Reservation (109.9°W, 36.5°N) of the Colorado Plateau and the Great Divide Basin (108°W, 42°N) within the Wyoming Basin (Fig. 4), while all other areas produce no effective dust emission. These isolated hotspots are some of the most effective producers of dust in North America, generating $F_{cal} > 1$ kg m^{-2} y^{-1}.

Dust emission sources over the high Central Rocky Mountains (Fig. 4) are not recognised by AOD data (e.g., Pu and Ginoux, 2017; Ginoux et al., 2012). Their omission emphasises the challenge of interpretating AOD aggregates over space and time, where fixed daily orbits of sun-synchronous satellites create a spatial bias, inherited from the transport component between the moment of emission and observation (Schepanski et al., 2012; Ashpole and Washington, 2013). The modelled F represent actual dust emission, rather than atmospheric dust which will be transported east along westerly winds (Jewell and Nicoll, 2011), where it is frequently observed in AOD measurements over the Great Plains (Pu and Ginoux, 2017), or removed entirely by rapid dry and wet deposition onto the Rocky Mountains (Reynolds et al., 2016; Munroe et al., 2019).

The Great Plains: Responding to regional variations in climate

Mean surface wind speeds over the Great Plains exceed those of the deserts and shrublands to the west (Fig. 5a). This occurs as dry and warm air masses follow westerly synoptic flow, descending the easterly slopes of the Rocky Mountains and creating Chinook winds (a type of foehn wind), accelerating wind speeds and increasing evaporation (MacDonald et al., 2018). The Western shortgrass prairie (WSP) ecoregion encompasses the semi-arid grasslands to the east of the Rocky Mountains. From the CW16 model, WSP produced 77% of all dust emission from the short grass prairie biome (2.2 Tg y^{-1}), the greatest of any ecoregion in North America. With winds speeds frequently high, F_{cal} magnitude corresponds to vegetation cover, with greatest dust emission (up to 2.1 kg m^{-2} y^{-1}) occurring across western rangelands, and cultivated croplands in the southwest (Fig. 4). These areas are frequently barren ($u_{s*}/U_h = 0.026$; Fig. 5), with cotton, corn, wheat, and sorghum crops rotated in line with seasonal precipitation, and left fallow during the dry (and windy) months between December and May (Rivera Rivera et al., 2010). Dust emission point source (DPS) observations increase frequency during periods of exceptional drought, as croplands remain barren for extended periods (Kandakji et al., 2021; Lee et al., 2009; Fig. 3). Further east, changes in climate conditions alter vegetation patterns over Texas, Oklahoma, and Kansas, as precipitation increases from ~ 250 mm in the west to >1000 mm in the east (Kukal and Irmak, 2016). Fig. 1c describes the climatic transition, with native short grasses and arable vegetation increasingly covering the landscape to east, decreasing $u_{s*}/U_h < 0.019$ (Figs. 4 and 5), reducing u_{s*} and prohibiting frequent dust emission despite limited change in mean wind speed.

Our results confirm previous findings that the roughness-limited dust emission pattern of the southern Great Plains increases the risk of soil loss in the second half of the 21st century. Here, historical precedents demonstrate the impact of changing vegetation patterns due to prolonged periods of drought. During the 1930s Dust Bowl event, the Southern High Plains in northern Texas and New Mexico suffered frequent severe dust storms due to a combination of drought conditions and damaging land use practices (Lee and Gill, 2015), causing both an environmental and socioeconomic crisis (Cook et al., 2009). Recently (2000–2014), IMPROVE time series data shows an increasing trend in spring-time dust concentrations in the southwest, with a strong inverse correlation with Pacific Decadal Oscillation (PDO) phase ($R = -0.65 p < 0.01$; Hand et al., 2016). During the second half of the 21st century, Coupled Model Intercomparison Project Phase 5 (CMIP5) models predict a decrease in springtime rainfall (Pu and Ginoux, 2017), with the potential for extensive and prolonged periods of drought ('megadroughts') (Cook et al., 2015). These conditions will increasingly stress existing arable and rangeland vegetation, in areas where grazing has increased by 2–10 times per head of cattle since the 1930s (Bolles et al., 2017) and dryland agriculture is expanding across multiple land cover types, including native grasslands in parts of west Kansas, and northwest Texas (Lark et al., 2015). Using the albedo-based dust emission modelling approach, we demonstrate for the first time how changing patterns in vegetation roughness during persistent Chinook (high) winds, alters u_{s*} (i.e., the wind friction force that controls sediment transport). This provides a useful indicator of how reduced vegetation will have a greater effect here, than in areas of lower or more variable wind patterns.

Summary and Conclusions

Using the albedo-based approach (CW16) we calculate spatial and temporal variability in wind friction velocity (u_{s*}) to model a dust emission climatology of North America during the period 2001 to 2020. Our results are calibrated through a novel use of dust emission point source (DPS) observations to accurately predict variability in dust emission frequency and magnitude. We compared dust emission from different ecological biomes (desert, shrubland, short, and tall grass prairies), as defined by patterns of vegetation type. These four EPA biomes are described by broad vegetation classification (Fig. 2). We represented that complexity and measured the proportion of shelter (as described by normalised shadow) within these land cover types, determining the relative aerodynamic roughness of these surfaces. We found comparable aerodynamic roughness exists across biomes/vegetation classes (Fig. 5b). Dust emission is not restricted to specific biomes, rather

to an 'envelope' of appropriate wind speed and vegetation roughness conditions that determine u_{s*}.

Calibrated modelled dust emission was restricted to the Great Plains and North American Deserts, with the greatest magnitude occurring in a central corridor surrounding the central Rocky Mountains, where semi-arid conditions and Chinook (foehn) winds coincide to create ideal conditions for frequent dust emission. Our results broadly agree with maps of frequently large aerosol optical depth, and ground station observations, yet our results provide greater accuracy of the variability in dust emission frequency, specifically the spatial and temporal coincidence of vegetation and wind conditions.

Calibrated modelled dust emission in the Great Plains is limited by fluctuations in roughness, occurring only over areas of small vegetation roughness (Fig. 4) as winds were strong enough to produce dust emission most of the time (roughness limited) (Fig. 5). In contrast, dust emission over North American Deserts is wind speed limited, occurring only in exposed areas where wind speeds peak (Fig. 4) as surface roughness is small most of the time (wind limited; Fig. 5).

We identified two distinct dust emission patterns from either side of the Rocky Mountains. Across the barren environments of the southwest, u_{s*} and therefore dust emission is limited only by patterns of wind speed, increasing over exposed areas where wind speeds peak (wind limited system). Across the vast semi-arid rangelands of the Great Plains, mean wind speeds remain high, with u_{s*} varying mostly due to fluctuations in roughness, limiting dust emission to the most barren environments (roughness limited system; Fig. 5). Despite these general patterns, each of the biomes had internal variability in frequency and magnitude of dust emission, which can be explained by spatial variations in u_{s*}/U_h and U_h at the ecoregion and smaller scales.

These data support previous findings, which suggest the southern Great Plains (e.g., the Southern High Plains) are most at risk of increasing dust emission in response to climate change. We show for the first time, how this increased threat is brought about by alterations in u_{s*}. Where, in a roughness limited environment, more frequent and longer duration droughts (as predicted in southern Great Plains in the second half of the 21st century) dramatically disrupts the balance between wind and vegetation roughness, altering the geography of dust emission frequency and magnitude, affecting the socioeconomical conditions of surrounding communities.

Funding

The work was produced whilst NPW and AC were funded by a joint grant from the US National Science Foundation and the UK Natural Environmental Research Council (EAR-1853853).

CRediT authorship contribution statement

Mark Hennen: Writing – original draft, Methodology, Software, Conceptualization, Data curation, Visualization, Investigation. **Adrian Chappell:** Conceptualization, Writing – review & editing, Funding acquisition, Supervision, Software, Methodology. **Brandon L. Edwards:** Conceptualization, Writing – review & editing, Funding acquisition. **Akasha M. Faist:** Writing – review & editing, Funding acquisition. **Tarek Kandakji:** Data curation. **Matthew C. Baddock:** Data curation. **Brandi Wheeler:** Writing – review & editing. **Gayle Tyree:** Writing – review & editing. **Ronald Treminio:** Writing – review & editing. **Nicholas P. Webb:** Conceptualization, Writing – review & editing, Funding acquisition.

Declaration of Competing Interest

The authors declare that they have no known competing financial interests or personal relationships that could have appeared to influence the work reported in this paper.

Acknowledgements

We are grateful to Google for access to and use of the Google Earth Engine (GEE) and support from Noel Gorelick and coding advice from GEE forum members. We also thank the following organisations for the use of their data: ECMWF Climate Reanalysis, ERA5-Land hourly; NASA EOSDIS Land Processes Distributed Active Archive Center (LP DAAC), USGS/Earth Resources Observation and Science (EROS) Center, Sioux Falls, South Dakota; ISRIC SoilGrids. We are grateful to Prof. Jeff Lee for providing dust emission point source data.

References

Ashpole, I., Washington, R., 2013. A new high-resolution central and western Saharan summertime dust source map from automated satellite dust plume tracking. J. Geophys. Res. Atmosph. 118 (13), 6981–6995.

Baddock, M.C., Gill, T.E., Bullard, J.E., Acosta, M.D., Rivera Rivera, N.I., 2011. Geomorphology of the Chihuahuan Desert based on potential dust emissions. J. Maps. 7 (1), 249–259.

Bestelmeyer, B.T., Okin, G.S., Duniway, M.C., Archer, S.R., Sayre, N.F., Williamson, J.C., Herrick, J.E., 2015. Desertification, land use, and the transformation of global drylands. Front. Ecol. Environ. 13 (1), 28–36.

Bolles, K., Forman, S.L., Sweeney, M., 2017. Eolian processes and heterogeneous dust emissivity during the 1930s Dust Bowl Drought and implications for projected 21st-century megadroughts. Holocene 27 (10), 1578–1588.

Breshears, D.D., Myers, O.B., Meyer, C.W., Barnes, F.J., Zou, C.B., Allen, C.D., McDowell, N.G., Pockman, W.T., 2009. Research communications research communications Tree die-off in response to global change-type drought: Mortality insights from a decade of plant water potential measurements. Front. Ecol. Environ. 7 (4), 185–189.

Carboni, E., Thomas, G.E., Sayer, A.M., Siddans, R., Poulsen, C.A., Grainger, R.G., Ahn, C., Antoine, D., Bevan, S., Braak, R., Brindley, H., Desouza-Machado, S., Deuzé, J.L., Diner, D., Ducos, F., Grey, W., Hsu, C., Kalashnikova, O.V., Kahn, R., North, P.R.J., Salustro, C., Smith, A., Tanré, D., Torres, O., Veihelmann, B., 2012. Intercomparison of desert dust optical depth from satellite measurements. Atmos. Meas. Tech. 5 (8), 1973–2002.

Chappell, A., Webb, N.P., 2016. Using albedo to reform wind erosion modelling, mapping and monitoring. Aeolian Res. 23, 63–78.

Cook, B.I., Ault, T.R., Smerdon, J.E., 2015. Unprecedented 21st century drought risk in the American Southwest and Central Plains. Sci. Adv. 1 (1), 1–8.

Cook, B.I., Miller, R.L., Seager, R., 2009. Amplification of the north american 'Dust Bowl' drought through human-induced land degradation. PNAS 106 (13), 4997–5001.

Darmenova, K., Sokolik, I.N., Shao, Y., Marticorena, B., Bergametti, G., 2009. Development of a physically based dust emission module within the weather research and forecasting (WRF) model: Assessment of dust emission parameterizations and input parameters for source regions in central and east asia. J. Geophys. Res. Atmosph. 114 (14), 1–28.

Dinerstein, E., Olson, D., Joshi, A., Vynne, C., Burgess, N.D., Wikramanayake, E., Hahn, N., Palminteri, S., Hedao, P., Noss, R., Hansen, M., Locke, H., Ellis, E.C., Jones, B., Barber, C.V., Hayes, R., Kormos, C., Martin, V., Crist, E., Sechrest, W., Price, L., Baillie, J.E.M., Weeden, D., Suckling, K., Davis, C., Sizer, N., Moore, R., Thau, D., Birch, T., Potapov, P., Turubanova, S., Tyukavina, A., De Souza, N., Pintea, L., Brito, J.C., Llewellyn, O.A., Miller, A.G., Patzelt, A., Ghazanfar, S.A., Timberlake, J., Klöser, H., Shennan-Farpón, Y., Kindt, R., Lillesø, J.P.B., Van Breugel, P., Graudal, L., Voge, M., Al-Shammari, K.F., Saleem, M., 2017. An Ecoregion-Based Approach to Protecting Half the Terrestrial Realm. Bioscience 67 (6), 534–545.

Dubovik, O., Smirnov, A., Holben, B.N., King, M.D., Kaufman, Y.J., Eck, T.F., Slutsker, I., 2000. Accuracy assessments of aerosol optical properties retrieved from Aerosol Robotic Network (AERONET) Sun and sky radiance measurements. J. Geophys. Res. Atmosph. 105 (D8), 9791–9806.

Eck, T.F., Holben, B.N., Reid, J.S., Dubovik, O., Smirnov, A., O'Neill, N.T., Slutsker, I., Kinne, S., 1999. Wavelength dependence of the optical depth of biomass burning, urban, and desert dust aerosols. J. Geophys. Res. 104 (D24), 31333–31349.

Edwards, B.L., Webb, N.P., Brown, D.P., Elias, E., Peck, D.E., Pierson, F.B., Williams, C.J., Herrick, J.E., 2019. Climate change impacts on wind and water erosion on US rangelands. J. Soil Water Conserv. 74 (4), 405–418.

Eibedingil, I.G., Gill, T.E., Van Pelt, R.S., Tong, D.Q., 2021. Comparison of Aerosol Optical Depth from MODIS Product Collection 6.1 and AERONET in the Western United States. Remote Sensing. 13 (12), 2316. https://doi.org/10.3390/rs13122316.

Fécan, F., Marticorena, B., Bergametti, G., 1999. Parametrization of the increase of the aeolian erosion threshold wind friction velocity due to soil moisture for arid and semi-arid areas. Ann. Geophys. 17 (1), 149–157.

Field, J.P., Belnap, J., Breshears, D.D., Neff, J.C., Okin, G.S., Whicker, J.J., Painter, T.H., Ravi, S., Reheis, M.C., Reynolds, R.L., 2010. The ecology of dust. Front. Ecol. 8 (8), 423–430.

Frank, T.D., Di Girolamo, L., Geegan, S., 2007. The spatial and temporal variability of aerosol optical depths in the Mojave Desert of southern California. Remote Sens. Environ. 107 (1-2), 54–64.

Ginoux, P., Prospero, J.M., Gill, T.E., Hsu, N.C., Zhao, M., 2012. Global-scale attribution of anthropogenic and natural dust sources and their emission rates based on MODIS Deep Blue aerosol products. Rev. Geophys. 50 (3), 1–36.
Goudie, A.S., 1983. Dust storms in space and time. Prog. Phys. Geogr. 7 (4), 502–530.
Goudie, A.S., Middleton, N.J., 1992. The changing frequency of dust storms through time. Clim. Change 20 (3), 197–225.
Hand, J.L., Gill, T.E., Schichtel, B.A., 2017. Spatial and seasonal variability in fine mineral dust and coarse aerosol mass at remote sites across the United States. J. Geophys. Res. 122 (5), 3080–3097.
Hand, J.L., White, W.H., Gebhart, K.A., Hyslop, N.P., Gill, T.E., Schichtel, B.A., 2016. Earlier onset of the spring fine dust season in the southwestern United States. Geophys. Res. Lett. 43 (8), 4001–4009.
Hennen, M., White, K., Shahgedanova, M., 2019. An assessment of SEVIRI imagery at various temporal resolutions and the effect on accurate dust emission mapping. Remote Sensing. 11 (8), 918. https://doi.org/10.3390/rs11080918.
Hereford, R., Webb, R.H., Longpré, C.I., 2006. Precipitation history and ecosystem response to multidecadal precipitation variability in the Mojave Desert region, 1893–2001. J. Arid Environ. 67 (SUPPL.), 13–34.
Huneeus, N., Schulz, M., Balkanski, Y., Griesfeller, J., Prospero, J., Kinne, S., Bauer, S., Boucher, O., Chin, M., Dentener, F., Diehl, T., Easter, R., Fillmore, D., Ghan, S., Ginoux, P., Grini, A., Horowitz, L., Koch, D., Krol, M.C., Landing, W., Liu, X., Mahowald, N., Miller, R., Morcrette, J.-J., Myhre, G., Penner, J., Perlwitz, J., Stier, P., Takemura, T., Zender, C.S., 2011. Global dust model intercomparison in AeroCom phase i. Atmos. Chem. Phys. 11 (15), 7781–7816.
Jewell, P.W., Nicoll, K. (2011) Wind regimes and aeolian transport in the Great Basin, U. S.A. *Geomorphology*.
Kandakji, T., Gill, T.E., Lee, J.A., 2021. Drought and land use/land cover impact on dust sources in Southern Great Plains and Chihuahuan Desert of the U.S.: Inferring anthropogenic effect. Sci. Total Environ. 755, 142461. https://doi.org/10.1016/j.scitotenv.2020.142461.
Kandakji, T., Gill, T.E., Lee, J.A., 2020. Identifying and characterizing dust point sources in the southwestern United States using remote sensing and GIS. Geomorphology 353, 107019. https://doi.org/10.1016/j.geomorph.2019.107019.
Kukal, M., Irmak, S., 2016. Long-term patterns of air temperatures, daily temperature range, precipitation, grass-reference evapotranspiration and aridity index in the USA Great Plains: Part I. Spatial trends. J. Hydrol. 542, 953–977.
Lark, T.J., Meghan Salmon, J., Gibbs, H.K., 2015. Cropland expansion outpaces agricultural and biofuel policies in the United States. Environ. Res. Lett. 10 (4), 044003. https://doi.org/10.1088/1748-9326/10/4/044003.
LaRue, E.A., Hardiman, B.S., Elliott, J.M., Fei, S., 2019. Structural diversity as a predictor of ecosystem function. Environ. Res. Lett. 14 (11), 114011. https://doi.org/10.1088/1748-9326/ab49bb.
Lee, J.A., Baddock, M.C., Mbuh, M.J., Gill, T.E., 2012. Geomorphic and land cover characteristics of aeolian dust sources in West Texas and eastern New Mexico, USA. Aeolian Res. 3 (4), 459–466.
Lee, J.A., Gill, T.E., 2015. Multiple causes of wind erosion in the Dust Bowl. Aeolian Res. 19, 15–36.
Lee, J.A., Gill, T.E., Mulligan, K.R., Dominguez Acosta, M., Perez, A.E., 2009. Land use/land cover and point sources of the 15 December 2003 dust storm in southwestern North America. Geomorphology 105 (1-2), 18–27.
Li, J., Kandakji, T., Lee, J.A., Tatarko, J., Blackwell, J., Gill, T.E., Collins, J.D., 2018. Blowing dust and highway safety in the southwestern United States: Characteristics of dust emission "hotspots" and management implications. Sci. Total Environ. 621, 1023–1032.
Li, J., Okin, G.S., Herrick, J.E., Belnap, J., Munson, S.M., Miller, M.E., Vest, K., Draut, A. E., 2013. Evaluation of a new model of aeolian transport in the presence of vegetation. J. Geophys. Res. 118, 1–19.
Marshall, J.K., 1971. Drag measurements in roughness arrays of varying density and distribution. Agric. Meteorol. 8, 269–292.
Marticorena, B., Bergametti, G., 1995. Modeling the atmospheric dust cycle: 1. Design of a soil-derived dust emission scheme. J. Geophys. Res. 100 (D8), 16415–16430.
Muñoz Sabater, J. (2019) ERA5-Land hourly data from 1981 to present. Copernicus Climate Change Service (C3S) Climate Data Store (CDS). doi:10.24381/cds.e2161bac, 2019.
Munroe, J.S., Norris, E.D., Carling, G.T., Beard, B.L., Satkoski, A.M., Liu, L. (2019) Isotope fingerprinting reveals western North American sources of modern dust in the Uinta Mountains, Utah, USA. *Aeolian Research*.
Nauman, T.W., Duniway, M.C., Webb, N.P., Belnap, J. (2018) Elevated aeolian sediment transport on the Colorado Plateau, USA: The role of grazing, vehicle disturbance, and increasing aridity. Earth Surface Processes and Landforms. doi:10.100.
Okin, G.S., Bullard, J.E., Reynolds, R.L., Ballantine, J.-A., Schepanski, K., Todd, M.C., Belnap, J., Baddock, M.C., Gill, T.E., Miller, M.E., 2011. Dust: small scale processes with global consequences. EOS. 92 (29), 241–242.
Omernik, J.M., 1987. Ecoregions of the Conterminous United States. Ann. Assoc. Am. Geogr. 77 (1), 118–125.
Orgill, M.M., Sehmel, G.A., 1976. Frequency and diurnal variation of dust storms in the contiguous U.S.A. Atmos. Environ. 10 (10), 813–825.
Painter, T.H., Skiles, S.M., Deems, J.S., Brandt, W.T., Dozier, J., 2018. Variation in rising limb of Colorado River snowmelt runoff hydrograph controlled by dust radiative forcing in snow. Geophys. Res. Lett. 45 (2), 797–808. https://doi.org/10.1002/grl.v45.210.1002/2017GL075826.
Pimentel, D., 2000. Soil erosion and the threat to food security and the environment. Ecosystem Health. 6 (4), 221–226.
Prospero, J.M., Ginoux, P., Torres, O., Nicholson, S.E., Gill, T.E., 2002. Environmental characterization of global sources of atmospheric soil dust identified with the Nimbus 7 Total Ozone Mapping Spectrometer (TOMS) absorbing aerosol product. Rev. Geophys. 40 (1), 2-1–2-31.
Pu, B., Ginoux, P., 2017. Projection of American dustiness in the late 21st century due to climate change. Sci. Rep. 7 (1), 1–10.
Ravi, S., Breshears, D.D., Huxman, T.E., D'Odorico, P., 2010. Land degradation in drylands: Interactions among hydrologic-aeolian erosion and vegetation dynamics. Geomorphology 116 (3-4), 236–245.
Reynolds, R.L., Munson, S.M., Fernandez, D., Goldstein, H.L., Neff, J.C., 2016. Concentrations of mineral aerosol from desert to plains across the central Rocky Mountains, western United States. Aeolian Res. 23, 21–35.
Rivera Rivera, N.I., Gill, T.E., Bleiweiss, M.P., Hand, J.L., 2010. Source characteristics of hazardous Chihuahuan Desert dust outbreaks. Atmos. Environ. 44 (20), 2457–2468.
Rivera Rivera, N.I., Gill, T.E., Gebhart, K.A., Hand, J.L., Bleiweiss, M.P., Fitzgerald, R.M., 2009. Wind modeling of Chihuahuan Desert dust outbreaks. Atmos. Environ. 43 (2), 347–354.
Schepanski, K., 2018. Transport of mineral dust and its impact on climate. Geosciences (Switzerland). 8 (5), 151. https://doi.org/10.3390/geosciences8050151.
Schepanski, K., Tegen, I., Macke, A., 2012. Comparison of satellite based observations of Saharan dust source areas. Remote Sens. Environ. 123, 90–97.
Sweeney, M.R., McDonald, E.V., Etyemezian, V., 2011. Quantifying dust emissions from desert landforms, eastern Mojave Desert, USA. Geomorphology 135 (1-2), 21–34.
UNEP UNCD, W.M.O. (2016) Global Assessment of Sand and Dust Storms. United Nations Environment Programme. Nairobi.
Webb, Nicholas P., Kachergis, Emily, Miller, Scott W., McCord, Sarah E., Bestelmeyer, Brandon T., Brown, Joel R., Chappell, Adrian, Edwards, Brandon L., Herrick, Jeffrey E., Karl, Jason W., Leys, John F., Metz, Loretta J., Smarik, Stephen, Tatarko, John, Van Zee, Justin W., Zwicke, Greg, 2020. Indicators and benchmarks for wind erosion monitoring, assessment and management. Ecol. Ind. 110, 105881. https://doi.org/10.1016/j.ecolind.2019.105881.
Webb, Nicholas P, Marshall, Nadine A, Stringer, Lindsay C, Reed, Mark S, Chappell, Adrian, Herrick, Jeffrey E, 2017a. Land degradation and climate change: building climate resilience in agriculture. Front. Ecol. Environ. 15 (8), 450–459.
Webb, N.P., Okin, G.S., Brown, S., 2014. The effect of roughness elements on wind erosion: The importance of surface shear stress distribution. J. Geophys. Res. [Atmos.] 119, 6066–6084.
Webb, Nicholas P., Pierre, Caroline, 2018. Quantifying Anthropogenic Dust Emissions. Earth's Future 6 (2), 286–295.
Webb, Nicholas P., Van Zee, Justin W., Karl, Jason W., Herrick, Jeffrey E., Courtright, Ericha M., Billings, Benjamin J., Boyd, Robert, Chappell, Adrian, Duniway, Michael C., Derner, Justin D., Hand, Jenny L., Kachergis, Emily, McCord, Sarah E., Newingham, Beth A., Pierson, Frederick B., Steiner, Jean L., Tatarko, John, Tedela, Negussie H., Toledo, David, Scott Van Pelt, R., 2017b. Enhancing wind erosion monitoring and assessment for US rangelands. Rangelands. 39 (3-4), 85–96.
Zobeck, T.M., Baddock, M.C., Van Pelt, R.S., 2013. 11.20 Anthropogenic Environments. Treat. Geomorphol. 11, 395–413.